Appl. Phys. A (2016) 122:1053
DOI 10.1007/s00339-016-0578-6

Applied Physics A
Materials Science & Processing

Photoluminescence properties of zinc white: an insight into its emission mechanisms through the study of historical artist materials

A. Artesani[1] · S. Bellei[1] · V. Capogrosso[1] · A. Cesaratto[3] · S. Mosca[1] · A. Nevin[2] · G. Valentini[1] · D. Comelli[1]

Received: 6 July 2016 / Accepted: 17 November 2016 / Published online: 28 November 2016

Abstract While the photophysical properties of ZnO nanostructures have been widely explored, less research has focused on the bulk material present in artist pigments. This study is based on the analysis of historical pastels, representative of artist materials available at the turn of the twentieth century, and of the pure powder pigment as the control sample. The study of the intensity of the photoluminescence emission as a function of the fluence and of the nanosecond and microsecond emission decay kinetic properties allows the elucidation of the emission mechanisms in control ZnO and historical samples containing ZnO. Data suggest that in historical samples the near-band-edge free-exciton photoluminescence emission, typically occurring in the pure semiconductor, is influenced by the interaction of the pigment with surrounding organic binding material. Conversely, crystal defects, typically expected in historical samples following the imperfect synthesis process available at the beginning of the twentieth century, introduce minor modifications to the photoluminescence emission. The study further suggests that zinc carboxylates, detected in all historical samples and known to introduce characteristic groups on the surface of ZnO, could be responsible for changes in emission mechanisms. Research demonstrates how photoluminescence decay kinetics and the study of the dependence of the emission intensity on the fluence are powerful methods for elucidating the nature of the mechanism processes in luminescent semiconductor pigments.

1 Introduction

Zinc as a mineral has been known since antiquity, but historians agree that it was first used as a white pigment in the form of zinc oxide (ZnO) only at the end of the eighteenth century. The ZnO-based pigment, despite some initial concerns of its quality, substituted the lead white mainly because of its non-toxicity and its intense whiteness, and it was manufactured all over the world [1]. Zinc white was produced mainly via three processes: the indirect (or French) process, which produced the oxide by burning zinc metal in air, the direct (or American) process, which involved smelting zinc ore in a furnace [2], and the less common wet chemical process, in which ZnO was produced from purified solutions of other zinc-based compound [3]. The final pigment achieved with the three synthesis methods has different chemical properties and composition. Generally, the French process yields a very pure pigment (with a typical composition of ZnO in 99.69–99.99 wt% and trace concentrations of Pb, Cd and Fe) [4]. Conversely, the direct process was widely noted for its simplicity, low cost and excellent thermal efficiency, but it produced a less pure form of ZnO (purity $> 98.5\%$) with a variety of possible impurities, including Pb, Cd, Fe, S, Cu and Mn [5]. Significant traces of Pb, Cd and S are also associated with the pigment produced through the wet process [4, 6].

Electronic supplementary material The online version of this article (doi:10.1007/s00339-016-0578-6) contains supplementary material, which is available to authorized users.

✉ A. Artesani
alessia.artesani@polimi.it

[1] Dipartimento di Fisica, Politecnico di Milano, Piazza Leonardo da Vinci 32, 20133 Milan, Italy

[2] Istituto di Fotonica e Nanotecnologie - Consiglio Nazionale delle Ricerche (IFN-CNR), Milan, Italy

[3] Department of Scientific Research, The Metropolitan Museum of Art, New York, NY, USA

In its pure form, ZnO is a semiconductor belonging to II–VI group and has two main crystalline forms. The hexagonal structure (wurtzite) is the most stable at ambient conditions and therefore the most common with band gap energy of 3.37 eV (368 nm) at room temperature. The second structure is the cubic one (zincblende), typically formed at high pressure [7] and for this reason less common, with a lower absorption edge energy (2.7 eV, 459 nm). In the 1970s, ZnO gained substantial interest for its optoelectronics applications as a potential material for light emitting devices [8, 9]. Subsequently, interest in ZnO has been motivated as it is a promising material for the synthesis of a variety of nanostructures and nanostructured devices [10].

One of the most suitable ways to study the energy levels of semiconductors is through photoluminescence (PL) spectroscopy [11]. ZnO exhibits different PL bands: one corresponding to an emission near the band-edge (NBE) in the UV region, while a broad band in the visible region is due to emission from trap states (TS) caused by intrinsic defects and impurities in the crystal structure. One of the most common TS emissions is centred in the green spectral region (around 5200 nm). The source of this green luminescence was first attributed to extrinsic defects incorporated in synthesis processes, particularly Cu ions [12]. At present this hypothesis is questioned and many agree that various centres may be simultaneously involved in green luminescence, principally intrinsic defects such as interstitial or vacancies of zinc and oxygen [13].

In order to obtain a pictorial material, ZnO, as a powder, is dispersed in a binder typically of lipidic or proteinaceous nature and, in commercial paint or pastels, is mixed with additives. Pictorial binders allow the insoluble pigment to bind and adhere to a pictorial surface. Clearly, ZnO as a white pigment or embedded in painted layers has a much more complex matrix than that of the pure semiconductor material. However, only few works have focused on the PL of ZnO paint. For example, Clementi et al. [14] studied the PL properties of zinc oxide in oil paints; it was reported that the direct recombination emission of the white pigment is notably enhanced in intensity by interactions with lipid binders, suggesting that this was caused by covalent bonds between zinc atoms and carboxylates (known also as zinc soaps). On the contrary, the green emission was poorly specific and possibly overlapped with the emission of the binding medium. With the aid of synchrotron-based PL microscopy [15, 16], it has been shown that historical ZnO-based samples, which emitted homogeneously on the macroscale in the region 490–510 nm, were spatially inhomogeneous on the sub-micrometre scale with the addition of specific PL signals at 410 and 425 nm. It has been suggested that these emissions, ascribed to defect-induced states within the band gap, could be indicative of manufacturing processes or long-term alterations of the pigment. Hence, zinc-based pigments present additional issues with respect to the pure semiconductor material which merit further studies.

Here, we have applied an in-depth study of the PL properties of ZnO-based historical pastels and of the pure zinc white pigment, used as a reference sample. The study is based on the recovery of the lifetimes of the different PL emission mechanisms and on the study of the dependence of the PL emission intensity on the fluence. With respect to traditional PL spectroscopy, both approaches provide quantitative information correlated with the presence of competitive radiative and non-radiative decay paths and allow the elucidation of the nature of the PL mechanism processes in semiconductor materials and pigments [17–19].

2 Materials and methods

2.1 Samples

Twelve historical Zn-based samples from the beginning of the twentieth century have been investigated. The samples, produced by Lefranc & Bourgeois, are in the form of pastel fragments of different hues (Table 1; Fig. 1). A reference sample was prepared by pressing zinc white (Kremer Pigmente GmbH) in powder form as a pellet (in the following, labelled as control ZnO). The significance of this group of samples relies on the fact that they are representative of complex modern painting materials, produced after the second Industrial Revolution by one of the most important pigment producers.

2.2 Methods

2.2.1 Raman spectroscopy

Analysis was performed using a portable Raman spectrometer [20] to detect the molecular bulk composition of samples. The device is based on a 785-nm CW laser source and a spectrometer, mounting a 600 grooves/mm grating and coupled to a front-illuminated cooled CCD. The system allows the detection of Raman peaks in the spectral range 150–3000 cm^{-1} with a spectral resolution close to 15 cm^{-1}. The laser and the spectrometer are connected through optical fibres to the probe, working in back-scattering geometry. The working distance is $\sim$3 mm, while the spot size on the sample is 50 μm in diameter. The power density on samples has always been kept below 1500 W cm^{-2}. Following spectral calibration and baseline correction, each spectrum is treated with the mathematical subtracted shift Raman spectroscopy (SSRS) method (with a spectral shift of 15 cm^{-1}) [21–23] to reduce the

Table 1 Spectroscopic analyses of historical and commercial samples

Sample	Hue	XRF	FE-SEM	Raman	FTIR	Identification
S01	White	**Zn**. Fe, Co, Ni, Ca	**ZnO, ZnS**. Al, Si, Ca, Cu	ZnO (438 cm^{-1}) (s) wax (1064 cm^{-1}) (m) linseed oil (1157, 1085 cm^{-1})	Zinc stearate wax linseed oil	Zinc white* zinc sulphide
S02		**Zn**. Fe, Co, Ni, Pb	**ZnO, ZnS**. Al, Si, Cu			
S03			**ZnO, ZnS**. Al, Cu Ca localized			
S04		**Zn**. Fe, Co, Ni, Ba	**ZnO, ZnS**. Al, Si, Ca, Cu, Fe			
S05	Lilac	**Zn, Mn**. Fe, Co, Ni, Ca, (Ba)	**ZnO, ZnS**. Al, P, Mn	ZnO (438 cm^{-1}) (s) wax (1064 cm^{-1}) (m) linseed oil (1157, 1085 cm^{-1})	Zinc stearate wax linseed oil Manganese violet	Zinc white* manganese violet
S06	Pale pink	**Zn**. Fe, Co, Ni	**ZnO, ZnS**. Al, Si, Ca, Cu Mg, K, Fe	ZnO (438 cm^{-1}) (s) wax (1064 cm^{-1}) (m) linseed oil (1157, 1085 cm^{-1})	Zinc stearate wax linseed oil	Zinc white* zinc sulphide Lake pigment
S07	Red	**Zn, Hg**. Fe, Co, Ni, S, Ca	**ZnO, ZnS**. Al, Si, Ca, Cu Hg, S correlated	HgS (252, 343 cm^{-1}) (vs.)		Zinc white* zinc sulphide Cinnabar
S08	Blue	**Zn**. Fe, Co, Ni, S, Ca	Not measured	Ultramarine (548 cm^{-1}) (vs.)	Zinc stearate wax linseed oil Ultramarine	Zinc white* ultramarine blue
S09	Green	**Zn, As, Cu**. Fe, Co, Ni	**ZnO, ZnS**. Al As, Cu correlated	ZnO (438 cm^{-1}) (s) wax (1064 cm^{-1}) (m) linseed oil (1157, 1085 cm^{-1})	Zinc stearate wax linseed oil Emerald green	Zinc white* zinc sulphide Emerald green
S10	Light grey	**Zn**. Fe, Co, Ni, Ca, Ba	Not measured	ZnO (438 cm^{-1}) (s) wax (1064 cm^{-1}) (m) linseed oil (1157, 1085 cm^{-1}) Carbon black (1325 cm-1) (br vs)	Zinc stearate wax linseed oil	Zinc white* carbon Black
S11			**ZnO, ZnS, $BaSO_4$** Al, Si, P, Cu Ca localized			Zinc white* zinc sulphide Lithopone carbon Black
S12	Red	**Zn, Fe**. Co, Ni, (Ba)	**ZnO, ZnS, $BaSO_4$**. Al, Si, Ca, Cu Fe	Fe_2O_3 (222 cm^{-1}) (vs) wax (1064 cm^{-1}) (m)		Zinc white* zinc sulphide Lithopone Fe-red pigment lake pigment
ZnO	White	**Zn**. Fe, Co, Ni	**ZnO**. Al	ZnO (438 cm^{-1}) (s)	Zinc oxide	Zinc oxide

Elements or compounds with strong signals are highlighted in bold, and other trace elements are reported. Some elements are listed in parentheses because their presence is unsure. If not specified, elements revealed with FE-SEM analysis were uniformly distributed, otherwise they are marked as localized or correlated if they are present as spots alone or localized in the same spatial position of other elements. The intensity of Raman peaks is specified using the usual symbols (*s* strong, *m* medium, *w* weak, *v* very, *sh* shoulder, *br* broad). Note that the peak at 438 cm^{-1} of ZnO with Raman is not always visible because of the luminescence in some pigments (S07, S08 and S12). In 'Identification' column, we have called zinc white* the basic composition zinc oxide, wax and linseed oil

Fig. 1 Colour picture of the historical samples

fluorescence background which is combined with Raman vibrations in the spectrum. The Raman spectrum is reconstructed by integrating the SSRS profile. The identification of pigments is finally achieved through comparison with Raman spectra from published databases [24, 25].

2.2.2 XRF spectroscopy

Measurements on samples were carried out using a portable X-ray fluorescence (XRF) spectrometer (Elio, XGLab srl) to detect their elemental bulk composition. The instrument is a fast system with a large-area silicon drift detector (SDD) (25 mm^2). The excitation source works with a Rh anode (Lα emission line at 2.69 keV), and the beam is collimated to a spot diameter on the sample of about 1.3 mm. The spectrometer detects elements from Na to Ur with an energy resolution below 135 eV, whereas lighter elements cannot be detected since the spectral region below 3 keV is covered by the intense emission of Rh tube. For all measurements, the following experimental conditions have been used: working distance $\sim$1.4 cm, tube voltage = 40 kV, tube anode current = 100 A, acquisition time = 40 s. XRF spectra of all samples have been processed in order to identify the detected emission lines. For the purpose, we have used the PyMCA software [26], based on a nonlinear least-squares fitting procedure which optimizes zero, gain, noise and Fano factors for the entire fitting region and for all XRF peaks simultaneously. The background was estimated with the strip background model.

2.2.3 FE-SEM

Morphologies and microstructure of samples were imaged with a field-emission scanning electron microscope (FE-SEM) designed for high vacuum operational mode (Tescan-Mira High Resolution Schottky FE-SEM). Working at 30 kV acceleration voltage allowed to achieve 1.2 nm as resolution for secondary electrons. The same system was used for energy-dispersive X-ray (EDX) analysis to map distribution of selected elements, allowing the inspection of the spatial correlation between two or more elements. Samples were prepared for FE-SEM/EDX analysis by removing very little material from the surface of pastel grains and subsequently depositing it onto carbon tape adhesive tabs. The FE-SEM method allows also the reconstruction of the mean elemental composition of samples in the analysed field of view (100 $\times$ 100 µm). In comparison with the bulk elemental composition detected with XRF spectroscopy, the method is also sensitive to lighter elements.

2.2.4 FTIR

Microsamples from the pastels were collected and analysed by Fourier transform infrared spectroscopy (FTIR), using a Nicolet 6700 spectrophotometer coupled with Nicolet Continuum FTIR microscope equipped with an MCT detector (acquired between 4000 and 600 cm^{-1} with 128 acquisitions and 4 cm^{-1} resolution) and equipped with a microcompression diamond cell. The spectra were baseline corrected using Omnic software and normalized on the intensity of the CH_3 stretching vibration (at about 2910 cm^{-1}).

2.2.5 Time-resolved photoluminescence spectroscopy

The system is based on a pulsed laser and on a fast-gated intensified camera coupled to a spectrometer. The camera is capable of high-speed gating to capture the decay kinetic of PL emission spectra. Excitation of PL from samples is provided by the third harmonic of a Q-switching Nd:YAG laser, emitting sub-ns pulses at 355 nm (CryLas FTSS 355-50, Crylas GmbH, Berlin, Germany) at a repetition rate of 100 Hz. The laser light is delivered to the sample through a multimode silica fibre (600 µm core). An optical probe allows the excitation of the PL signal from sample surface in a circular spot of 1 mm in diameter with a maximum fluence per pulse of 10^2µJ cm^{-2} equivalent to an average power density of 0.1 W cm^{-2}. PL emission from samples is collected in a back-scattering geometry and focused into the entrance slit of an imaging spectrometer. The spectrometer (Acton Research 2300i, focal length = 300 mm, *f*/4 aperture) mounts a 150-lpmm grating and enables us to record PL spectra in the spectral range 380–700 nm with a spectral resolution of 10 nm. The kinetics of the emission is detected by a gated intensified camera (C9546-03, Hamamatsu Photonics, Japan), mounted at the exit port of the spectrometer. The detector features an acquisition gate adjustable from 3 ns to continuous mode. A custom-built trigger unit and a precision delay generator complete the system, which has a temporal jitter close to 500 ps. The measurement procedure is based on the detection of a sequence of PL-gated spectra at different delays with

respect to the laser pulses. In this work, the NBE emission was detected by employing a gate width of 5 ns and properly sampling the first 30 ns of the decay kinetic. Emission from TS levels was detected with a gate width of 1 μs and recording the long-lived decay kinetic in the first 20 μs. In the last configuration, a long-pass filter (SCHOTT 400 nm) was placed in the collection path to remove the NBE emission. Following proper calibration of spectral data and correction for the detector efficiency, it is possible to observe PL spectra from the samples in a selected temporal gate window (in the following quoted as gated spectra) or to observe the emission decay kinetic in a proper spectral window. In the latter case, a multiexponential decay (with a maximum of three components) was fitted to the kinetic data integrated over a selected spectral region [27], using a nonlinear least-squares fitting methods applied to the model function:

$$f(x) = \sum_{i=1}^{3} A_i \tau_i \left(1 - e^{-w/\tau_i}\right) e^{-t/\tau_i} \quad (1)$$

where τ_i and A_i are the lifetime and the intensity of the ith decay component, respectively, while w is the width of the experimental gate. The effective lifetime is then calculated as the average of the lifetimes weighted over the number of photons originating from each decay path, according to the equation:

$$\tau_{\text{eff}} = \frac{\Sigma_i A_i \tau_i^2}{\Sigma_i A_i \tau_i} \quad (2)$$

2.2.6 PL spectroscopy at different fluences

PL spectroscopy was performed by employing a CW compact spectrometer and the same 355-nm pulsed laser source employed for TRPL measurements. The compact spectrometer (TM-CCD C10083CA-2100, Hamamatsu Photonics) mounts a back-thinned CCD image sensor and a transmission-type grating, which allows the recording of spectra in the range 320–1100 nm with a spectral resolution of 6 nm. Through fibre optics, both the laser and the spectrometer are connected to a remote optical probe, working in the 45°–0° configuration. The probe focuses the excitation light as a spot of approximately 1 mm in diameter on the sample at a distance of 35 mm and collects the fluorescence emission as well. The optical probe is equipped with a variable neutral density filter that allows the variation of the fluence of two orders of magnitude: in the present case, fluence on samples was varied from 0.1 to 1 μJ cm^{-2} . PL spectra are reported following background subtraction (achieved by acquiring the detected signal with the laser switched off) and correction for the spectral efficiency of the device.

2.2.7 Analysis of PL and TRPL-gated spectra

PL spectra and TRPL-gated spectra are always shown following correction for self-absorption phenomena in coloured samples on the basis of a Kubelka–Munk correction model described elsewhere [28]. The diffuse reflectance $R(\lambda)$ of the samples at all emission wavelengths and at the 355-nm excitation, required for applying the correction model, was collected with a visible reflectance spectroscopy device. This device is based on the same set-up employed in steady-state PL spectroscopy by substituting the UV laser source with a fibre-coupled halogen lamp (Lamp HL-2000-HR) having a nominal output power of 8.4 mW. Reflectance spectra of samples were determined using a diffusive reference sample (Spectralon Labsphere 0D074-2298). Following correction for self-absorption phenomena PL and TRPL-gated spectra, linked to the visible emission from trap state levels in the ZnO samples, were deconvoluted as the sum three Gaussian shape functions to provide a rough discrimination of decay paths originating from different TS levels. Peak positions of the three Gaussian functions were retrieved by applying a nonlinear fitting procedure, based on the minimization of the χ^2 error, while the spectral width of the Gaussian function was kept fixed at a third of the total spectral width of the visible emission. This constrain was necessary to better interpolate the curves in terms of errors of fitting parameters.

3 Results

3.1 Preliminary characterization of samples in terms of composition

Results of preliminary analyses are summarized in Table 1, and all spectra data (XRF, Raman and FTIR) plus SEM images are shown in Supplementary Material. The historical samples all contain zinc oxide (ZnO), in some cases zinc sulphide (ZnS), probably added as an extender of the white pigment, and wax and linseed oil as binders. The different hues of pastels were achieved with the addition of coloured pigments, in most cases easily identified by Raman and XRF spectroscopy: Carbon Black in grey pastels (S10, S11), Ultramarine Blue and Emerald Green in the blue (S08) and green pastels (S09), respectively. Reddish hues were achieved with the addition of Cinnabar (S07), Manganese violet (S05) and a Fe-based red pigment (S12). Interestingly, FE-SEM analysis showed the presence of Ca, K, S in S06 and in S12. These elements are usually correlated with the presence of a lake pigment that could also contribute to the colour of these samples.

Trace element impurities were further detected. For example, XRF highlighted Fe, Co and Ni in all samples, and Ca and Ba in some of them. Complementary, FE-SEM analysis detected elements uniformly distributed within the samples, such as Al and Cu, while others are more localized. The most complex composition was found in samples labelled S06, S12. A lower but still significant number of elements were also detected in samples S03 and S04. These samples contain, in addition to the elements cited above, traces of Mg, Si and P. These trace elements can be related to the presence of other pigments, added to achieve a specific hue, or to impurities unintentionally introduced during the imperfect synthesis processes. FE-SEM images of samples are shown in Supplementary Material and reveal very fine particles of ZnO distributed in an organic matrix, which vary with sample in concentration and morphology. The control sample has the finest particle size.

FTIR analysis, besides confirming the presence of wax and a drying oil, detected zinc stearate in all historical samples. This compound might be an additive, or more often it is associated with the formation and aggregation of zinc soaps [29, 30].

Finally, it is worth noting that the control ZnO sample was found to be quite pure, containing only Al impurities revealed by FE-SEM analysis and traces of Fe, Co and Ni highlighted by XRF analysis.

3.2 Photoluminescence spectroscopy

PL spectra of all samples, shown in Fig. 2, were detected upon an excitation fluence of 10 μJ cm^{-2}. Samples show a narrow emission band in the near-UV and a broad emission band in the green spectral range associated, respectively, with radiative recombination from the band-edge (BE) and via trap state (TS) levels. In terms of the spectral shape of the NBE emission, all samples share similar features: a narrow emission peaked at 382.7 nm with a FWHM around 13.2 in the control sample, and a close emission peaked at 382.3 nm (±0.4, 1σ) with a FWHM around 12.5 nm (±0.1, 1σ) in all historical samples.

The TS emission is more complex. In historical samples, we detected an emission centred at 530 nm with significant variation among samples, such as the FWHM and its relative intensity with respect to the NBE, as shown in Fig. 2. Conversely, in control ZnO the TS emissions less intense than that in historical samples. Further, it is red shifted with a broad emission centred at 570 nm. The broad TS emission detected in all samples is clearly the superposition of the emission from a variety of trap state levels close each other. In order to provide a simple decomposition for this broad emission, PL spectra of all samples were fitted as the sum of three Gaussian components, with maxima at 490 nm (TS1), 530 nm (TS2) and 570 nm (TS3). Despite the slight differences among samples in the peak position and weight of each Gaussian contribution, every interpolation resulted in a good 2 value, always higher than 0.999 (Table SM2). As an explanatory example, the fit result for sample S02 is reported in Supplementary Material: experimental data appear to be perfectly reproduced by the sum of three Gaussian functions with a prediction bound of 1 sigma, and the fitting residuals being lower than 2% than the intensity of the emission. Similar fitting results have been achieved for all the other samples (data not shown).

We systematically investigated the fluence dependency of NBE and TS emission for the control ZnO sample and a representative selection of five historical samples (those characterized by the most different chemical composition). It is worth noting that at the maximum employed excitation fluence (10^2 μJ cm^{-2}), we have not detected any photo-induced effect and any visible modification or darkening of samples, as expected for the stable crystalline structures of semiconductors. First, the NBE emission in all samples has a non-symmetric quasi-Gaussian shape

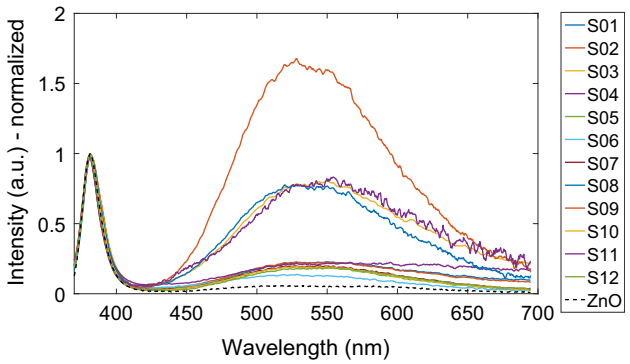

Fig. 2 Photoluminescence spectra acquired with 355 nm excitation for historical samples (*continuous lines*) and control sample (*dashed line*) under fluence of 10 μJ cm^{-2}. Spectra are corrected for self-absorption and instrumental efficiency

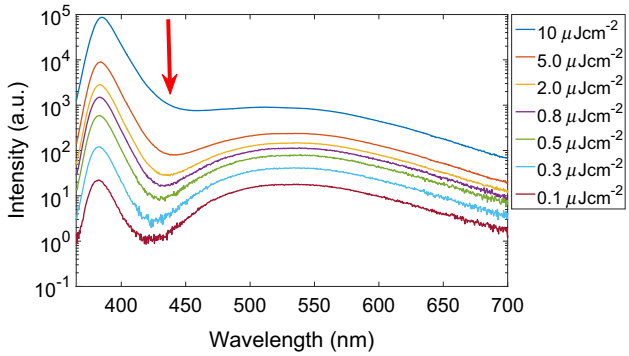

Fig. 3 PL spectra of control ZnO as a function of fluence, from 10 to 0.1 μJ cm^{-2}. At higher fluence, the shoulder of the NBE emission (indicated with a *yellow arrow*) is observed, yielding an apparent *red* shift of the NBE peak position of 3 nm

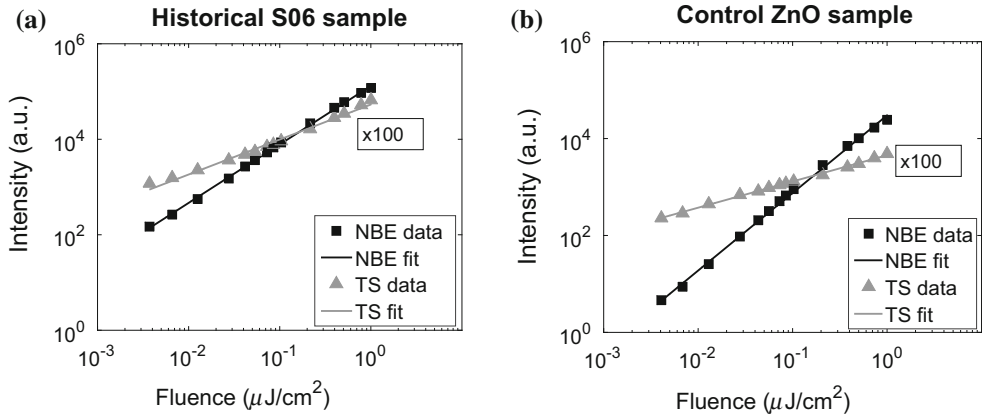

Fig. 4 PL intensity (as total emitted counts) in the NBE spectral band peaked at 382 nm (*grey triangles*) and in the TS spectral band peaked at 530 nm (*black squares*) versus the fluence in log–log scale for **a** historical S06 sample and **b** control zinc oxide sample. For better visibility, data of TS intensity are multiplied by a factor of 100. The results of linear fitting of data in the log–log scale are reported as *continuous lines*

Table 2 Characteristic coefficients for NBE and TS emissions

	NBE		TS		
	k	τ_{eff} (ns)	k	τ_{eff} (μs)	$\hat{\lambda}$ (nm)
S01	1.35	1.27	0.74	2.66	530
S02	–	1.23	–	3.35	529
S03	1.40	1.68	0.66	3.84	533
S04	1.23	1.38	0.71	2.85	534
S05	–	1.22	–	3.23	531
S06	1.20	1.15	0.72	2.52	532
S07	–	1.38	–	2.99	534
S08	–	1.49	–	3.21	524
S09	–	1.00	–	4.18	523
S10	–	1.29	–	3.45	526
S11	–	1.18	–	3.86	525
S12	1.24	1.46	0.66	2.94	541
Average ($\pm\sigma$)	1.28 ± 0.09	1.31 ± 0.20	0.70 ± 0.04	3.26 ± 0.60	530 ± 5
ZnO	1.58	0.55	0.54	5.27	567

The coefficient k expresses the angular dependence of intensity on fluence in log–log scale ($\log(I) = \log(I_0) + k \cdot \log(F)$). The effective lifetime (τ_{eff}) is calculated following a nonlinear fit of (a) bi-exponential decay model for NBE ($\lambda = 390$ nm, $\Delta\lambda = 10$ nm) and (b) tri-exponential decay model for TS ($\lambda = 530, \Delta\lambda = 100$ nm). $\hat{\lambda}$ represents the centre of the TS emission band. The average value in historical samples of the coefficients is reported together with the variance (σ)

that becomes more evident at higher fluences. In fact, changing the fluence from 0.1 to 10 μJ cm^{-2}, the shoulder of the NBE emission increases at longer wavelengths yielding an apparent red shift of the NBE peak position of 3 nm (Fig. 3). This effect is present in both control and historical samples. The asymmetric shape of the NBE emission has been interpolated with two Gaussian functions, peaked at 382 nm and 390 nm. The latter peak is referred to as the blue emission (BL) from herein. Second, the intensity of the NBE and TS emission was plotted as a function of excitation fluence, and an example of the results is shown in Fig. 4 for sample S06 and control ZnO. Similar data were recorded from historical samples (data not shown). In plots on the log–log scale, it can be seen that the NBE emission intensity is more pronounced than the TS emission and this difference is more evident in the control sample. The slope of the log–log curve is reported in Table 2, following the modelling of data with the relationship $I = I_0 \cdot F^k$ (that in a log–log scale gives rise to a linear behaviour $\log(I) = \log(I_0) + k \log(F)$), where I is the emission intensity and F is the laser fluence on sample [17, 18].

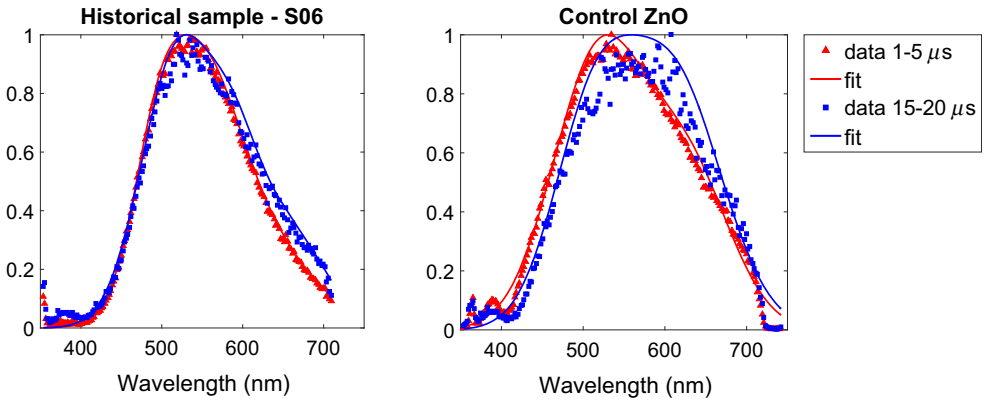

Fig. 5 Time-gated spectra of one historical sample (S06) and control ZnO sample. The *red line* is the interpolation for the emission gated in 1–5 μs, while the *blue line* is the interpolation for 15–20 μs gated spectra. Spectra are corrected for self-absorption and instrumental efficiency

Finally, TRPL spectroscopy analysis on all samples with an excitation fluence of 10^2 μJ cm^{-2} was performed to estimate the emission decay kinetics of the NBE and TS emissions. NBE emission gave rise to a nanosecond decay, which was well modelled with a bi-exponential decay. The full results of the fitted decay kinetic parameters are provided in Supplementary Material, whereas synthetic results, in terms of the effective lifetime, are reported in Table 2. It is noted that the lifetime values recorded from historical samples are comparable with an average value of $\tau_{eff} = 1.31$ ns, $\sigma = 0.20$ ns (with values ranging in the interval 1.0–1.7 ns), whereas control ZnO has a much shorter lifetime ($\tau_{eff} = 0.55$ ns).

For the TS emission, the use of a gated detector was particularly effective for the removal of the nanosecond emission from organic compounds in historical samples (such as that associated with organic binders and carboxylates [31]). In fact, emission from organic compounds, typically occurring in the visible spectral range, is spectrally superimposed with the visible TS emission and hence represents a serious limit to the proper analysis of trap state levels with conventional steady-state PL spectroscopy devices, as recognised previously. In all samples (historical and the control), the TS emission is characterized by decay kinetics with detectable differences in the different regions of the analysed spectral range. This confirms that the broad TS emission is actually the superposition of the contributions from different trap state levels, characterized by different trapping lifetimes. In particular, TRPL-gated spectra are slightly red shifted at longer delays, and the effect is most visible in the control sample (Fig. 5): from a physical point of view, this phenomenon suggests that the deepest traps (occurring at lower energy in the band gap and hence at longer emission wavelengths) have the slowest decay kinetic. The TS decay kinetic has been modelled as the sum of three exponential decay functions. Results, in terms of the effective lifetime detected in the whole spectral range, are reported in Table 2. Lifetime values are similar among historical samples varying between 2.5 and 4.2 μs and have an average value of $\tau_{eff} = 3.26$ μs ($\sigma = 0.60$ μs). In comparison, control zinc oxide has an effective lifetime for trap state emission of $\tau_{eff} = 5.27$ μs.

4 Discussion

Many studies have reported on the PL emission of ZnO, but at present, some of the photophysical properties of this semiconductor pigment in complex painted layers or in complex artist materials are still poorly understood. It is important to stress here that the recent literature on ZnO is primarily focused on the semiconductor employed as a nanomaterial, whereas few works deal with bulk ZnO. Erdem [32] reported a study on analogies and differences among photoluminescence produced by bulk and nanoparticles ZnO. The main result was that the latter produced a more intense emission in the green region, while for bulk materials the recombination via the conduction band is the strongest. Moreover, Djurisic and Leung [33] suggested that the defect behaviour in nanoparticle and bulk materials is similar and the main difference is the density of defects on the surface that is greater in nanoparticles.

Bearing in mind that the majority of contemporary literature deals with nanoparticle materials, we here discuss the current attribution for the green emission in ZnO. While the origin of photoluminescence in zinc oxide is contested, generally, the peak around 380 nm is associated with near-band-edge emission, while different defects are responsible for the green emission around 530 nm. This broad emission is well known in literature, and some hypotheses for its attribution have been suggested. Many agree that the main species responsible for the green

emission are oxygen and zinc vacancies (V_O and V_{Zn}) and interstitial defects of Zn (Zn_i). In studies on nanoparticles, Han et al. [34] have discriminated the emission from Zn_i to the valence band, which produces luminescence at 430 nm, and the emission from Zn_i to V_{Zn} which lead to emission at 480 nm. Other authors ascribe V_O as being mainly responsible for 530-nm emission [13, 35]. Interestingly, many recent studies achieved by combining experimental and computational simulation have pointed out that the green emission originates from surface intrinsic defects [36–38]. Apart from these simple findings, the analysis of the fluence dependence of the PL emission and the analysis of the PL emission lifetimes have provided additional information on the different recombination paths detected in control ZnO and historical samples, which are summarized and discussed below.

4.1 Control zinc oxide

The study of the behaviour of the PL intensity as a function of the fluence allows the identification of the underlying recombination process [17]. As a general result, it has been reported that the intensity of the NBE PL emission is proportional to F^k, where F is the fluence of the exciting laser radiation and $1 < k < 2$ for exciton-like transitions and $k < 1$ for free-to-bound and donor–acceptor pair transitions, respectively [17, 18]. Here, the dependency on fluence of the NBE emission was found to be over-linear with a characteristic coefficient of $k = 1.58$, which clearly suggests a free-exciton recombination path, as reported for other studies on pure ZnO samples [41]. The finding is confirmed by time-resolved PL analysis: the NBE emission of control ZnO has a sub-nanosecond lifetime, in very good agreement with data reported in the literature for ZnO as a thin film or single crystal, showing a typical lifetime value of 0.55–0.70 ns at 300 K temperature [39].

Recombinations via trap states are more complex. The k value for TS emission was less than one $k = 0.54$, suggesting a sub-linear dependency on fluence, which is characteristic of free-to-bound and donor–acceptor transitions originated from trap state levels in non-perfect crystals. Further, the detection of a microsecond decay kinetic confirms the nature of this green emission as originating from trapped electrons. More interestingly, in this broadband, ascribed to emission from a variety of trap state levels, the effective lifetime increases with increasing of wavelength and conversely the k value decreases, as reported in Table 3. This finding suggests that for recombination in deeper trap state levels (characterized by a PL emission occurring at longer wavelengths) trapped electrons are more stable (longer lifetime) and the related trap levels are less easily depopulated (lower k value). Even though it is not possible to provide an identification of the type of defects emitting at shorter/longer wavelengths in this broad visible band (with particular reference to defects related to Zn and O vacancies), it is worth noting that a similar behaviour of the k coefficient has been reported in reference [40], where the visible PL and cathodo-luminescence emission from Zn- and O-rich ZnO samples have been investigated. In both types of non-stoichiometric ZnO samples, the visible emission has a sub-linear dependence on fluence, with the emission observed in Zn-rich samples occurring at shorter wavelengths and with an intensity that increases at a significant faster rate than what observed in O-rich samples.

Finally, another result provided by the study of the PL emission as a function of fluence is that NBE emission is characterized by a second near emission (BL), with peak position around 390 nm that is enhanced with fluence intensity. The red shift of NBE emission with excitation is a known effect for semiconductors [34, 41]. This phenomenon might be due to shallow levels (on the order of 50 meV below the conduction band) that recombine directly with holes in the valence band. BL emissions in general are related to state levels which are particularly sensitive to temperature and irradiance conditions, while without stressing the system, they are basically negligible [42]. Indeed, the peculiarity of the NBE emission merits further study.

Table 3 Characteristic coefficients for TS

	k			τ_{eff} (μs)		
	TS1	TS2	TS3	TS1	TS2	TS3
Average	0.76	0.68	0.65	3.18	3.25	3.36
ZnO	0.59	0.52	0.54	5.01	5.23	6.04

k expresses the fluence dependence of intensity on fluence ($I = I_0 \cdot F^k$). Effective lifetime (τ_{eff}) is calculated following a non-linear fit of a three-exponential decay model in a selected spectral region window of 10 nm of width. Both k and τ_{eff} are evaluated for three different spectral bands: TS1 (490 nm), TS2 (530 nm) and TS3 (570 nm)

4.2 Historical zinc oxide

The PL emissions from our historical samples match results reported by others, which deal with the study of PL of zinc oxide as white pigment. In fact, we confirm the evidence of narrow peak at 390 nm and a broader green emission in region the 490–600 nm. Additionally, as explained in reference [16], the authors were able to detect a specific emission at 410 and 425 nm from localized spots at the sub-micrometre scale that was not achievable with our experimental set-up. The NBE PL emission of historical samples shows clear differences with respect to that observed in control ZnO in terms of emission mechanisms

as described below. The historical samples have a substantially higher effective lifetime value and an over-linear dependence of PL intensity on fluence with the value of the k coefficient smaller than the one retrieved in the control sample. These differences cannot be explained with reference to an increased number of competitive radiative and non-radiative recombination paths originating from the greater concentration of crystal defects expected in the less-perfect historical samples. In fact, it is well known that additional competitive paths give rise to a more rapid depopulation of the excited level (i.e. shorter lifetime) and to an increase in the k coefficient [43]. On the other hand, the increase in the lifetime of the NBE emission cannot be explained with the simple superposition of the optical emission from the organic matter present in historical samples, as the detected emission is still characterized by an over-linear dependence with the excitation intensity, which is typical of PL emission from semiconductors. Hence, it is supposed that the NBE emission, ascribed to free-exciton direct recombination in pure ZnO samples, follows a different near-band-edge emission mechanisms in historical samples, possibly introduced by the chemical interaction of the pigment with the organic binder and the formation of zinc carboxylates, which are well known to introduce characteristic groups on the surface of ZnO [43].

Regarding the PL emission ascribed to TS levels, as seen in control zinc oxide, the value of lifetime increases with increasing wavelength, while the k value decreases, as reported in Table 3. Hence, the same hypotheses advanced for the control sample can be drawn for historical samples. Indeed, the effective lifetime in historical sample was found to be smaller than that reported for the pure ZnO sample (with an average value of $\tau_{\text{eff}} = 3.26\ \mu\text{s}$), whereas the k value in historical samples ($k = 0.70$) is in general greater than the k value for the control ZnO ($k = 0.54$). Shibata et al. [18] have demonstrated that with decreasing crystal lattice perfection of the samples, the value of k for the free-to-bound or donor–acceptor transitions is expected to increase. This reference suggests that in historical samples the TS emission is modified by the presence of increasing decay paths, which in this case can be related to the increased number of defects expected in historical samples.

5 Conclusion

In this work, we have shown how it is possible to provide clear insights into the emission mechanism of the zinc white pigment by analysis of the emission intensity as a function of the fluence and of the nanosecond and microsecond emission decay kinetic. With respect to traditional steady-state PL spectroscopy analysis, our approach provides valuable information for a clearer attribution of the emission paths that could be extended to the analysis of the wide class of semiconductor luminescent pigments. In the case of the selected historical samples, we report weak, but detectable modifications in the microsecond TS emission with respect to those observed in the control sample. These changes could be ascribed to a greater concentration of crystal defects, typically expected in samples produced with the imperfect synthesis and grinding processes available at the turn of the twentieth century. More interestingly, whereas the peculiar NBE emission of pure ZnO can be ascribed to direct free-exciton recombination, in historical samples, where ZnO is mixed with a complex organic matrix, the mechanism responsible for the NBE emission shows a substantial change. We hypothesize that the detected variations of the NBE emission in historical samples could also be influenced by the presence of zinc carboxylates, which are well known to introduce characteristic groups on the surface of ZnO particles [43]. Zinc stearate is usually associated with degradation process in painted layers, and its effect on the physical and chemical stability of oil paint layers is a major issue [44, 45]. To better investigate this issue, we plan to study the interaction binder pigments in artificially aged samples through the PL emission, to probe the photophysical effects of degradation.

Acknowledgements Authors wish to thank the Central European Research Infrastructure Consortium (CERIC-ERIC) for measurements and analyses of FE-SEM and Francesca Gherardi from Chemistry Department of Politecnico di Milano for measurements and analyses of FTIR spectroscopy. We are grateful to Lucia Toniolo from Chemistry Department of Politecnico di Milano for providing us historical samples. Research was partially funded by the Italian Ministry of Education, Universities and Research within the framework of the JPI Cultural Heritage JHEP Pilot call through the LeadART project 'Induced decay and ageing mechanisms in paintings: focus on interactions between lead and zinc white and organic material'.

References

1. G. Osmond, Zinc white a review of zinc oxide pigment properties and implications for stability in oil based paintings. AICCM Bull. **33**, 20–29 (2012)
2. G. Buxbaum, *Industrial Inorganic Pigments, 281* (VCH, Weinheim, 1993)
3. D.B. Faloon, *Zinc Oxide: History, Manufacture and Properties as a Pigment* (Van Nostrand, 1925)
4. A. Moezzi, A.M. McDonagh, M.B. Cortie, Zinc oxide particles: synthesis, properties and applications. Chem. Eng. J. **185186**, 1–22 (2012)
5. F. Casadio, V. Rose, High-resolution fluorescence mapping of impurities in historical zinc oxide pigments: hard X-ray nanoprobe applications to the paints of Pablo Picasso. Appl. Phys. A **111**, 18 (2013)
6. V. Capogrosso, F. Gabrieli, S. Bellei, L. Cartechini, A. Cesaratto, N. Trcera, F. Rosi, G. Valentini, D. Comellia, A. Nevin, An integrated approach based on micro-mapping analytical techniques for the detection of impurities in historical Zn-based white pigments. J. Anal. At. Spectrom. **30**, 828–838 (2015)

7. P.A. Rodnyi, I.V. Khodyuk, Optical and luminescence properties of zinc oxide (review). Opt. Spectrosc. **111**, 776–785 (2011)
8. U. Özgür, D. Hofstetter, H. Morkoc, ZnO devices and applications: a review of current status and future prospects. Proc. IEEE **98**(7), 1255–1268 (2010)
9. C.W. Litton, D.C. Reynolds, T.C. Collins, *Zinc Oxide Materials for Electronic and Optoelectronic Device Applications* (Wiley, Hoboken, 2011). doi:10.1002/9781119991038
10. Ü. Özgür, Y. Alivov, C. Liu, A. Teke, M.A. Reshchikov, S. Doğan, V. Avrutin, S. Cho, H. Morkoc, A comprehensive review of ZnO materials and devices. J. Appl. Phys. **98**, 041301 (2005)
11. A. Alkauskas, M.D. McCluskeyn, C.G. Van de Walle, Tutorial: defects in semiconductors—combining experiment and theory. J. Appl. Phys. **119**, 181101 (2016)
12. N.Y. Garces, L. Wang, L. Bai, N.C. Giles, L.E. Halliburton, G. Cantwell, Role of copper in the green luminescence from ZnO crystals. Appl. Phys. Lett. **81**, 622–624 (2002)
13. T.M. Børseth, B.G. Svensson, A.Y. Kuznetsov, P. Klason, Q.X. Zhao, M. Willander, Identification of oxygen and zinc vacancy optical signals in ZnO. Appl. Phys. Lett. **89**, 262112 (2006)
14. C. Clementi, F. Rosi, A. Romani, R. Vivani, B.G. Brunetti, C. Miliani, Photoluminescence properties of zinc oxide in paints: a study of the effect of self-absorption and passivation. Appl. Spectrosc. **66**, 1233–1241 (2012)
15. M. Thoury, J.P. Echard, M. Réfrégiers, B. Berrie, A. Nevin, F. Jamme, L. Bertrand, Synchrotron UV–visible multispectral luminescence microimaging of historical samples. Anal. Chem. **83**, 1737–1745 (2011)
16. L. Bertrand, M. Réfrégiers, B. Berrie, J.P. Échard, M. Thoury, A multiscalar photoluminescence approach to discriminate among semiconducting historical zinc white pigments. Analyst **138**, 4463–4469 (2013)
17. T. Schmidt, K. Lischka, W. Zulehner, Excitation-power dependence of the near-band-edge photoluminescence of semiconductors. Phys. Rev. B **45**, 8989–8994 (1992)
18. H. Shibata, M. Sakai, A. Yamada, K. Matsubara, K. Sakurai, H. Tampo, S. Ishizuka, K. Kim, S. Niki, Excitation-power dependence of free exciton photoluminescence of semiconductors. Jpn. J. Appl. Phys. **44**, 6113 (2005)
19. S. Lettieri, V. Capello, L. Santamaria, P. Maddalena, On quantitative analysis of interband recombination dynamics: theory and application to bulk ZnO. Appl. Phys. Lett. **103**, 241910 (2013)
20. S. Mosca, T. Frizzi, M. Pontone, R. Alberti, L. Bombelli, V. Capogrosso, A. Nevin, G. Valentini, D. Comelli, Identification of pigments in different layers of illuminated manuscripts by X-ray fluorescence mapping and Raman spectroscopy. Microchem. J. **124**, 775–784 (2016)
21. S.E.J. Bell, E.S.O. Bourguignon, A. Dennis, Analysis of luminescent samples using subtracted shifted Raman spectroscopy. Analyst **123**, 17291734 (1998). doi:10.1039/a802802h
22. I. Osticioli, J. Raman Spectrosc. **37**, 974980 (2006)
23. F. Rosi, M. Paolantoni, C. Clementi, B. Doherty, C. Miliani, B.G. Brunetti et al., Subtracted shifted Raman spectroscopy of organic dyes and lakes. J. Raman Spectrosc. **41**, 452458 (2010). doi:10.1002/jrs.2447
24. RRUFF Project website. http://rruff.info (2016)
25. Raman Spectroscopic Library. http://www.chem.uc.ac.uk/resources/raman (2016)
26. V.A. Solé, E. Papillon, M. Cotte, P.H. Walter, J. Susini, A multiplatform code for the analysis of energydispersive X-ray fluorescence spectra. J. Spectrochim. Acta B **62**, 6368 (2007)
27. D. Comelli, A. Nevin, A. Brambilla, I. Osticioli, G. Valentini, L. Toniolo, M. Fratelli, R. Cubeddu, On the discovery of an unusual luminescent pigment in Van Gogh's painting 'Les bretonnes et le pardon de pont Aven'. Appl. Phys. A **106**, 25–34 (2012)
28. G. Verri, C. Clementi, D. Comelli, S. Cather, F. Piqueé, Correction of ultraviolet-induced fluorescence spectra for the examination of polychromy. Appl. Spectrosc. **62**, 1295–1302 (2008)
29. G. Osmond, J.J. Boonc, L. Puskard, J. Drennana, Metal stearate distributions in modern artists' oil paints: surface and cross-sectional investigation of reference paint films using conventional and synchrotron infrared microspectroscopy. Appl Spectrosc. **66**, 1136–1144 (2012)
30. L. Robinet, M.C. Corbeil, The characterization of metal soaps. Stud. Conserv. **48**, 23–40 (2003)
31. J.J. Boon, J. van der Weerd, K. Keune, P. Noble, J. Wadum, Mechanical and chemical changes in old master paintings: dissolution, metal soap formation and remineralization processes in lead pigmented ground/intermediate paint layers of seventeenth century paintings, in *13th Triennial Meeting Rio de Janeiro 22–27 September 2002: ICOM Committee for Conservation*, ed. by R. Vontobel (James & James, London, 2002), pp. 401–406
32. E. Erdem, Microwave power, temperature, atmospheric and light dependence of intrinsic defects in ZnO nanoparticles: a study of electron paramagnetic resonance (EPR) spectroscopy. J. Alloys Compd. **605**, 34–44 (2014)
33. A.B. Djurišić, Y.H. Leung, Optical properties of ZnO nanostructures. Small **2**(8–9), 944–961 (2006). doi:10.1002/smll.200600134
34. N.S. Han, H.S. Shim, J.H. Seo, S.Y. Kim, S.M. Park, J.K. Song, Defect states of ZnO nanoparticles: discrimination by time-resolved photoluminescence spectroscopy. J. Appl. Phys. **107**, 084306 (2010)
35. K. Kodama, T. Uchino, Thermally activated below-band-gap excitation behind green photoluminescence in ZnO. J. Appl. Phys. **111**, 093525 (2012)
36. F. Fabbri, M. Villani, A. Catellani, A. Calzolari, G. Cicero, D. Calestani, G. Calestani, A. Zappettini, B. Dierre, T. Sekiguchi, G. Salviati, Zn vacancy induced green luminescence on non-polar surfaces in ZnO nanostructures. Sci. Rep. **4**, 5158 (2014)
37. J.V. Foreman, J.G. Simmons, W.E. Baughman, J. Liu, H.O. Everitt, Localized excitons mediate defect emission in ZnO powders. J. Appl. Phys. **113**, 133513 (2013)
38. Z.G. Wang, X.T. Zu, S. Zhu, L.M. Wang, Green luminescence originates from surface defects in ZnO nanoparticles. Phys. E Low-Dimens. Syst. Nanostruct. **35**, 199 (2006)
39. M. Lorenz, R. Johne, T. Nobis, H. Hochmuth, J. Lenzner, M. Grundmann, H.P.D. Schenk, S.I. Borenstain, A. Schon, C. Bekeny, T. Voss, J. Gutowski, Fast, high-efficiency, and homogeneous room-temperature cathodoluminescence of ZnO scintillator thin films on sapphire. Appl. Phys. Lett. **89**, 243510 (2006)
40. C. Ton-That, L. Weston, M.R. Phillips, Characteristics of point defects in the green luminescence from Zn- and O-rich ZnO. Phys. Rev. B **86**, 115–205 (2012)
41. S.A. Studenikin, M. Cocivera, Time-resolved luminescence and photoconductivity of polycrystalline ZnO films. J. Appl. Phys. **91**, 5060–5065 (2002)
42. B.K. Meyer, H. Alves, D.M. Hofmann, W. Kriegseis, D. Forster, F. Bertram, J. Christen, A. Hoffmann, M. Strassburg, M. Dworzak, U. Haboeck, A.V. Rodina, Bound exciton and donor-acceptor pair recombinations in ZnO. Phys. Stat. Sol. **241**, 231–260 (2004)
43. A.K. Radzimska, T. Jesionowski, Zinc oxide—from synthesis to application: a review. Materials **7**, 2833–2881 (2014)
44. J.J. Hermans, K. Keune, A. Van Loon, P.D. Iedema, An infrared spectroscopic study of the nature of zinc carboxylates in oil paintings. J. Anal. At. Spectrom. **30**, 1600–1608 (2015)
45. G. Osmond, B. Ebert, J. Drennan, Zinc oxide-centred deterioration in 20th century Vietnamese paintings by Nguyen Trong Kiem (19331991). AICCM Bull. **34**, 4 (2014)

http://www.springer.com/978-3-662-55416-6

inArt 2016
2nd International Conference on Innovation in Art Research and Technology
Vandenabeele, P.; Bersani, D.; Candeias, A. (Eds.)
2017, VII, 401 p. 284 illus., 200 illus. in color.,
Hardcover
ISBN: 978-3-662-55416-6